Physics of the Earth and Planetary Interiors 233 (2014) 103–111

Contents lists available at ScienceDirect

Physics of the Earth and Planetary Interiors

journal homepage: www.elsevier.com/locate/pepi

Seismic structure and ultra-low velocity zones at the base of the Earth's mantle beneath Southeast Asia

Jiayuan Yao [a,*], Lianxing Wen [b,a]

[a] Laboratory of Seismology and Physics of Earth's Interior, University of Science and Technology of China, Hefei, Anhui 230026, China
[b] Department of Geosciences, State University of New York at Stony Brook, Stony Brook, NY 11794, USA

ARTICLE INFO

Article history:
Received 22 January 2014
Received in revised form 12 May 2014
Accepted 21 May 2014
Available online 29 May 2014

Keywords:
Seismic structure
Seismic scattering
ULVZ
Downwelling
Low-velocity region

ABSTRACT

We constrain seismic structure and ultra-low velocity zones near the Earth's core-mantle boundary (CMB) beneath Southeast Asia. We first determine the average shear-velocity structure near the CMB in the region based on travel-time analysis of S, ScS, P and ScP phases. We then map seismic scattering in the lowermost mantle using the PKP precursors observed at the USArray. The inferred average shear-velocity perturbations in the lowermost 200 km of the mantle range from about −6% to 6%, and exhibit a complex geographic distribution of alternate low- and high-velocity patches adjacent to each other, surrounded by a high-velocity anomaly in the south. The inferred strong seismic scatterers exhibit a crescent shape distributed from the South China Sea to the Maluku Islands and coincide with the westernmost low-velocity patch, suggesting that the strong scatterers represent ultra-low velocity zones (ULVZs). We suggest that the seismic structure in the region likely results from a complex interaction between a downwelling and a low-velocity region near the CMB. The downwelling (the high-velocity patches) displaces the low-velocity region into many low-velocity patches and pushes the ULVZs to the edge of the low-velocity region.

1. Introduction

The core-mantle boundary (CMB) is one of the most important interfaces in the Earth's interior and plays a key role in the geodynamical evolution of the planet. During the past two decades, many studies have reported existence of ultra-low velocity zones (ULVZs) at the CMB, which are characterized by zones of variable thickness of ~5–50 km with negative P and S velocity perturbations of 10% or greater (Garnero, 2000). Many localized ULVZs have been detected using anomalous SKS-SPdKS waveforms (Garnero and Helmberger, 1995; Jensen et al., 2013; Rondenay et al., 2010; Thorne and Garnero, 2004; Thorne et al., 2013; Wen and Helmberger, 1998a), PcP precursors (Hutko et al., 2009; Mori and Helmberger, 1995), ScP precursors and postcursors (Garnero and Vidale, 1999; Idehara, 2011; Idehara et al., 2007; Rost and Revenaugh, 2003), PKP precursors (Cormier, 1999; Frost et al., 2013; Niu and Wen, 2001; Thomas et al., 1999; Vidale and Hedlin, 1998; Wen, 2000; Wen and Helmberger, 1998b), ScS travel times and waveforms (Avants et al., 2006; He et al., 2006), S/Sdiff waveforms (Cottaar and Romanowicz, 2012), P and Pdiff slowness (Xu and Koper, 2009), and SKKS/SKS amplitude ratios (Zhang et al., 2009). The proposed explanations of ULVZs include partial melt either in the normal mantle (Williams and Garnero, 1996) or resulting from compositional changes (Rost et al., 2005; Wen, 2001), iron-rich post-perovskite (Mao et al., 2006) and iron-rich (Mg, Fe)O (Wicks et al., 2010).

Mapping the geographic presence of ULVZs and their relationship to the surrounding velocity structure would place important constraints on the origin of ULVZs, dynamical and chemical evolution of the Earth's mantle and origin of the hotspots (e.g., Helmberger et al., 1998; McNamara et al., 2010; Wen, 2000; Williams et al., 1998). Of particular interest are the interactions of ULVZs with prominent low-velocity anomalies in the lower mantle and mantle downwelling (McNamara et al., 2010). Thus far, ULVZs have been observed to be present in many CMB regions and most of the observed ULVZs lie inside or close to the low-velocity regions at the CMB (McNamara et al., 2010). The regions lacking evidence for ULVZs are typically associated with high shear-wave velocity regions (Williams et al., 1998). In relationship to two prominent low-velocity provinces in the lower mantle, He and Wen (2009, 2012) indicated that, while ULVZs are also present inside the Pacific Anomaly, many are located inside the basal portion of the Anomaly that extends beneath the surrounding high-velocity region; on the other hand, while Helmberger et al. (2000) and Thorne and Garnero (2004) reported evidence or high

* Corresponding author. Tel.: +86 15155514849.
E-mail address: kaka22yao@gmail.com (J. Yao).

http://dx.doi.org/10.1016/j.pepi.2014.05.009
0031-9201/

likelihood of ULVZs beneath eastern Atlantic and the south of Indian Ocean at the eastern edge of the African Anomaly, Wen (2001, 2002) and Wang and Wen (2007) suggested that there is no evidence of existence of ULVZs inside the Anomaly.

In this study, we focus on studying the relationship between the velocity structure and geographic distribution of ULVZs in the CMB region beneath Southeast Asia. The region is located close to the boundary of the Pacific Anomaly in the lower mantle (He and Wen, 2012; He et al., 2006; Simmons et al., 2010), and may have experienced complex interaction between the edge extension of the Anomaly and the surrounding high-velocity regions (presumably downwellings). Understanding the relationship between the velocity structure and geographic distribution of ULVZs in this region may provide insights into the interaction of mantle downwelling and the low-velocity structure at the CMB, and may further our understanding of the nature of the Pacific Anomaly. Few detailed studies of velocity structure are available in this region, but there are reports of some localized ULVZs based on ScP precursors and postcursors (Idehara, 2011; Idehara et al., 2007) and anomalous SPdKS waveforms (Jensen et al., 2013). In the present study, we first determine detailed shear-velocity structure near the CMB beneath this region based on travel-time analysis of S, ScS, P and ScP phases. We then constrain seismic scattering in the region on the basis of migration of PKP precursory energy observed at the USArray, and explore relationship between the seismic scattering and the inferred seismic velocity structure. We discuss detailed shear-velocity structure in section 2, seismic scattering results in section 3, and a possible explanation of the seismic structure in section 4.

2. Shear-velocity structure near the CMB beneath Southeast Asia

We use ScS travel-time residuals and ScS-S and ScP-P differential travel-time residuals to constrain the average shear-velocity structure near the CMB beneath the region. We first correct for the effects of shear-velocity heterogeneities in the mantle 200 km above the CMB for S wave legs and those of P velocity heterogeneities from the CMB to the surface for P wave legs from the observed ScS travel-time residuals and ScS-S and ScP-P differential travel-time residuals. We then infer the average shear-velocity perturbations near the CMB beneath the region based on the corrected travel-time residuals.

2.1. ScS and ScP data

We collect broadband tangential displacements of S and ScS phases recorded at a distance range between 40° and 85° for events occurring in the Sunda subduction zone from 1990 to 2013 with a magnitude greater than 5.6 and vertical displacements of P and ScP phases at a distance range between 40° and 60°. Seismic data are collected from the China Earthquake Network Center (CENC), the F-net in Japan and the database of the Incorporated Research Institutions for Seismology (IRIS) (Fig. 1a). The tangential and vertical waveforms are all deconvolved with their instrumental responses. The tangential waveforms recorded by CENC and other networks are bandpass-filtered from 0.08 to 1 Hz and 0.008 to 1 Hz, respectively. The vertical waveforms are bandpass-filtered from 0.5 to 1.5 Hz.

We choose 24 earthquakes for S and ScS travel-time analysis and 16 earthquakes for P and ScP travel-time analysis. We retain only the data with clear phase onsets and hand pick the onsets of those phases. We obtain a total of 240 ScS and S travel-time residuals and 264 ScP and P travel-time residuals with respect to PREM (Dziewonski and Anderson, 1981). The combined data

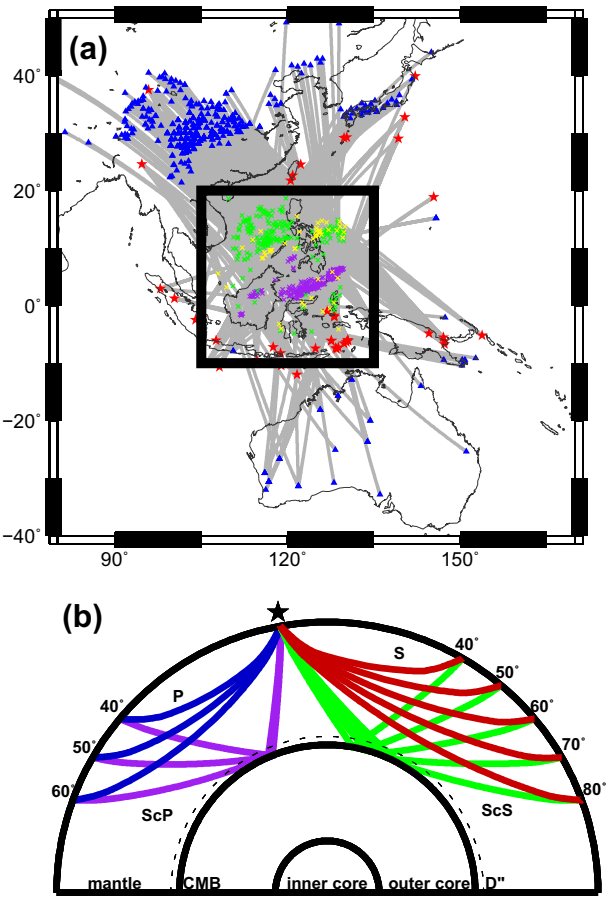

Fig. 1. (a) The CMB region of the shear-velocity study (black box) using ScS travel-time residuals and ScS-S and ScP-P differential travel-time residuals, along with earthquakes (red stars), seismic stations (blue triangles) and great circle paths (gray lines). Green (ScS travel-time residuals used) and yellow (ScS-S differential travel-time residuals used) crosses represent ScS reflection points at the CMB. Purple crosses represent the middle points of the S wave legs of ScP in the lowermost 200 km of the mantle. (b) Ray paths of direct S (red traces) and ScS (green traces) at epicentral distances from 40° to 80°, and direct P (blue traces) and ScP (purple traces) at epicentral distances from 40° to 60°. The example ray paths are calculated on the basis of PREM (Dziewonski and Anderson, 1981) and a surface source (For interpretation of the references to color in this figure legend, the reader is referred to the web version of this article.)

constitute good coverage near the CMB beneath the region, with ScS sampling the northern and southern parts of the region and ScP sampling the middle part (Fig. 1a).

2.2. Average shear-velocity structure near the CMB

It is common to use ScS-S and ScP-P differential travel-time residuals to constrain the seismic structure in the lowermost mantle, as these differential travel-time residuals would minimize the effects due to uncertainties of event location and origin time, and seismic heterogeneities in the upper mantle (Fig. 1b). However, along many ScS and S sample paths of this study (events with superscript c in Table 1), the S travel times are significantly affected by a high-velocity anomaly in the mid-lower mantle beneath the S turning points. This is reflected in these two observed travel-time patterns: (1) the observed absolute S travel times exhibit large negative residuals, and (2) the S travel-time residuals are negatively correlated with the ScS-S travel-time residuals, while the ScS residuals do not correlate with ScS-S differential travel-time residuals (see an example in Fig. 2a–d). For these reasons, for those ScS and S sampling paths, we choose to use ScS

Table 1
Event list.

Year Month Day	Hour Min Sec	Latitude (°N)	Longitude (°E)	Depth (km)	Magnitude ($m_{b)}$
1999/11/11[b]	18:05:43.5	1.28	100.32	211	6.0
2001/02/16[b]	05:59:09.5	−7.16	117.49	521	5.9
2004/04/17[b]	15:58:24.6	−7.35	128.37	129	6.1
2004/07/25[c]	14:35:19.1	−2.43	103.98	582	6.8
2004/10/13[b]	20:35:41.0	−6.07	130.53	90	5.9
2005/12/03[d]	16:10:39.6	29.34	130.29	26	6.1
2006/12/26[c]	12:26:21.1	21.80	120.55	10	6.4
2007/06/26[c]	22:23:07.8	−10.65	108.12	17	5.8
2007/08/08[a,c]	17:05:11.3	−6.03	107.58	305	6.1
2007/10/31[d]	03:30:16.0	18.90	145.39	207	6.2
2008/04/29[b,c]	19:10:05.3	−6.08	127.61	412	5.6
2008/08/04[b]	20:45:19.7	−5.93	130.47	174	6.1
2008/08/30[c]	06:54:07.6	−6.15	147.26	75	6.1
2008/11/10[d]	01:22:02.6	37.57	95.83	19	6.4
2008/11/10[a]	08:58:51.4	−0.28	100.23	128	5.3
2008/12/06[a,b]	10:55:31.5	−7.44	124.84	407	6.1
2009/01/22[b]	20:16:37.8	−7.51	128.55	160	6.1
2009/02/19[a]	09:03:24.9	−7.44	120.83	596	4.9
2009/03/07[a]	16:27:22.4	−8.59	123.68	169	5.6
2009/06/07[a]	05:25:27.2	−8.60	118.47	146	5.0
2009/06/23[d]	14:19:22.4	−5.16	153.78	64	6.3
2009/08/12[c]	22:48:51.4	32.82	140.40	53	6.2
2009/08/28[a]	01:51:25.9	−7.09	123.46	634	6.2
2009/10/03[d]	17:36:06.1	23.63	121.45	28	6.0
2009/11/08[b]	19:41:51.0	−8.21	118.76	20	6.7
2009/11/28[c]	06:04:22.2	−10.40	118.89	15	5.9
2010/02/15[a]	21:51:48.0	−7.26	128.79	128	6.2
2010/03/14[b]	00:57:44.7	−1.69	128.14	53	6.3
2010/04/17[c]	23:15:22.0	−6.67	147.29	53	6.2
2010/04/24[b]	07:41:00.4	−1.91	128.12	27	6.0
2010/12/01[a]	00:50:21.0	2.62	99.04	161	5.5
2010/12/15[b]	11:29:30.0	−7.25	128.82	133	5.9
2010/12/23[a]	16:28:14.0	−8.04	119.95	203	5.7
2011/02/04[c]	13:53:46.3	24.62	94.68	85	6.4
2011/03/10[a]	17:08:36.0	−6.86	116.76	508	6.5
2011/06/22[d]	21:50:52.4	39.96	142.21	33	6.1
2011/06/27[a]	16:47:15.0	−8.95	122.51	129	5.8
2011/07/08[a]	05:22:40.0	0.10	123.28	152	5.6
2011/07/16[a]	17:06:39.0	−7.10	127.55	246	5.8
2011/09/05[a,d]	17:55:13.0	2.97	98.00	110	6.6
2011/10/13[b]	03:16:29.0	−9.38	114.63	35	6.1
2011/11/14[b]	04:05:11.4	−0.95	126.91	17	6.2
2011/11/15[a]	07:56:02.0	7.50	127.83	163	5.5
2011/11/15[a]	10:43:50.0	−0.13	121.93	263	5.8
2011/11/28[a]	09:13:10.9	−7.01	117.00	613	5.9
2011/12/13[a]	07:52:12.0	−0.07	123.10	161	6.3
2012/01/20[a]	20:32:53.5	−8.41	119.70	127	5.7
2012/02/26[d]	02:35:00.5	22.66	120.89	28	5.9
2012/04/17[c]	07:13:49.0	−5.46	147.12	198	6.5
2012/06/09[d]	21:00:18.1	24.57	122.25	70	6.0
2012/08/19[d]	22:41:49.8	−4.77	144.57	73	6.0
2012/09/08[b]	10:51:44.2	−3.18	135.11	21	6.2
2012/10/23[c]	08:53:38.2	29.06	139.25	436	6.0
2012/12/10[b]	16:53:08.8	−6.53	129.82	155	6.6
2013/04/19[c]	17:51:41.4	−11.98	121.63	15	6.0
2013/04/20[d]	04:51:12.0	−6.29	130.22	108	6.0

[a] PKP precursors are used.
[b] ScP-P differential travel-time residuals are used.
[c] ScS travel-time residuals are used.
[d] ScS-S differential travel-time residuals are used.

residuals, instead of ScS-S differential travel-time residuals, to constrain the seismic velocity structure in the lowermost mantle. For the other ScS and S sampling paths with good correlation between ScS residuals and ScS-S differential travel-time residuals (events with superscript d in Table 1 and see an example in Fig. 2e–h), we use ScS-S differential travel-time residuals. Along the ScP and P sampling paths, we use ScP-P differential travel-time residuals (events with superscript b in Table 1), as the P wave travel times do not show any evidence for existence of significant anomalies in the mid-lower mantle along those P wave paths.

Before we attribute the observed travel-time residuals to shear-velocity perturbations in the lowermost mantle, we need to remove the travel-time contributions from the seismic heterogeneities in the rest of the mantle. We estimate such travel-time contributions by summing the travel-time anomalies along the ray path of the seismic phase in the portion of the mantle for correction, based on a tomographic model. The ray paths of all the phases are calculated based on actual event depths. He and Wen (2012) tested five tomographic models for correcting travel-time residuals due to seismic heterogeneities 500 km above the CMB along the

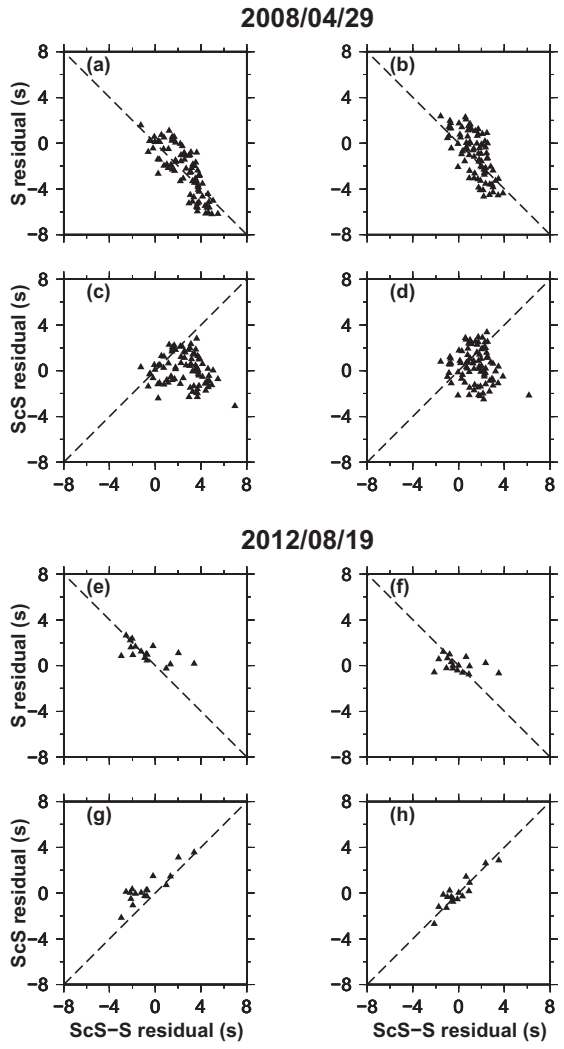

Fig. 2. (a–d) An example (event 2008/04/29) of relationship between observed S travel-time residuals and ScS-S differential travel-time residuals (a) before and (b) after the corrections for the effects of the seismic heterogeneities 200 km above the CMB based on tomographic model GyPSuM (Simmons et al., 2010), and between observed ScS travel-time residuals and ScS-S differential travel-time residuals (c) before and (d) after corrections. The dashed lines intercept at (0,0) and have a slope of −1 in panels (a–b) and a slope of 1 in panels (c–d). (e–h) Same as (a–d) except for event 2012/08/19.

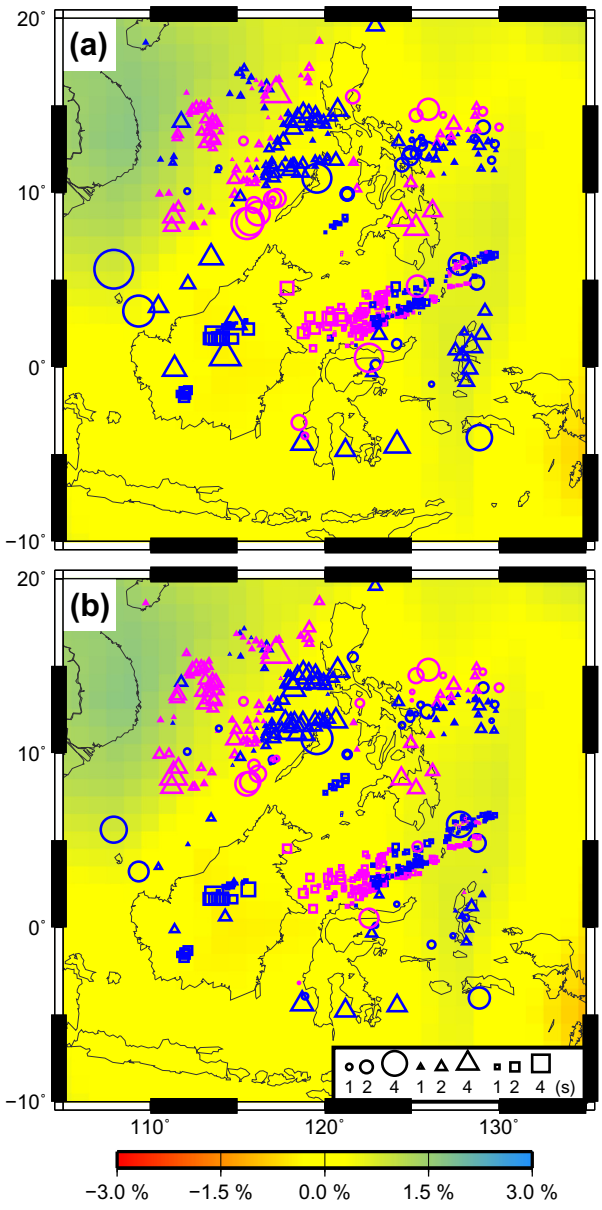

Fig. 3. Observed ScS travel-time residuals (triangles) and ScS-S differential travel-time residuals (circles) plotted at the ScS reflection points at the CMB and ScP-P differential travel-time residuals (squares) at the middle points of the S wave legs of ScP in the lowermost 200 km of the mantle, (a) before and (b) after corrected for the effects of the mantle heterogeneities. Positive and negative residuals are plotted as red and blue symbols, with sizes of the symbols proportional to the magnitudes of the residuals. The S wave legs are corrected for the effects of shear-velocity heterogeneities 200 km above the CMB and the P wave legs are corrected for the effects of P velocity heterogeneities from the CMB to the surface using tomographic model GyPSuM (Simmons et al., 2010). Background is shear-velocity perturbations at the CMB from GyPSuM model. (For interpretation of the references to color in this figure legend, the reader is referred to the web version of this article.)

seismic paths sampling the Pacific Anomaly. They chose GyPSuM model (Simmons et al., 2010) because that model produced the best correlation between ScS and ScS-S travel-time residuals after corrections. As the region we study is near the Pacific Anomaly, we also choose GyPSuM model for travel-time correction. For ScS travel-time residuals and ScS-S differential travel-time residuals, we remove the travel-time contributions caused by the shear-velocity heterogeneities 200 km above the CMB. For ScP-P differential travel-time residuals, we remove the travel-time contributions caused by the shear-velocity heterogeneities 200 km above the CMB for the S wave legs and the P velocity heterogeneities from the CMB to the surface for the P wave legs. Thus, we consider the corrected ScP-P differential residuals are contributed by the S wave legs of the ScP phases in the lowermost 200 km of the mantle. The corrected travel-time residuals exhibit a similar geographic pattern as the original data, with a slight change of magnitude (Figs. 2 and 3a, b).

The corrected travel-time residuals are the integral effects of the shear-velocity anomalies in the lowermost mantle. In the present case, the ScS and ScP travel-time data alone do not have resolution to constrain the vertical extent of the anomaly in the lowermost mantle; the magnitude of the inferred velocity perturbation trade-offs with the assumed vertical extent of the anomaly. So, we attribute the corrected ScS travel-time residuals and ScS-S and ScP-P differential travel-time residuals to lateral variations of shear-velocity in the lowermost 200 km of the mantle and estimate the magnitude of the shear-velocity perturbations in the lowermost 200 km of the mantle based on the corrected residuals (Fig. 3b). The shear-velocity perturbations are inferred based on formula $\delta v/v = \delta t/v$, where δt is the corrected travel-time

residual, t is the travel-time ScS or the S wave leg of ScP propagates through the bottom 200 km of the mantle, and v is the average shear-velocity in the lowermost 200 km of the mantle. The inferred shear-velocity perturbations are then projected to the bouncing points of ScS or the middle points of the S wave legs of ScP in the lowermost 200 km of the mantle. The actual velocity perturbations would scale with the actual vertical extent of the seismic anomalies in the lowermost mantle beneath the region.

The inferred shear-velocity perturbations are further averaged over 1° × 1° grids (Fig. 4). The inferred average velocity perturbations range from about −6% to 6%, and exhibit a complex geographic distribution of alternate low- and high-velocity patches adjacent to each other, surrounded by a high-velocity anomaly in the south (Fig. 4). Such complex features of seismic heterogeneities are not present in the current global tomography models. For example, while GyPSuM model shows two high-velocity regions in the northwest and southeast areas of the study region, it exhibits no seismic heterogeneities in the portion of the CMB where the alternative low and high-velocity patches are found in this study (Fig. 4).

3. Seismic scattering near the CMB from PKP precursors

We utilize the observed PKP precursory energy to determine seismic scattering in the lowermost mantle beneath the region. PKP precursors are caused by seismic scattering in the lowermost mantle (Cleary and Haddon, 1972; Doornbos and Husebye, 1972; Haddon and Cleary, 1974; Husebye et al., 1976) (Fig. 5a). The arrival time of precursor depends on depth and lateral location of the scatterer and the amplitude of the precursor is controlled by magnitude and geometry of the scatterer. The PKP precursors have been used to constrain small-scale seismic heterogeneities in the lowermost mantle and yielded many insights into the nature of the lowermost mantle (Cormier, 1999; Frost et al., 2013; Hedlin et al., 1997; Niu and Wen, 2001; Thomas et al., 1999; Vidale and Hedlin, 1998; Wen, 2000; Wen and Helmberger, 1998b).

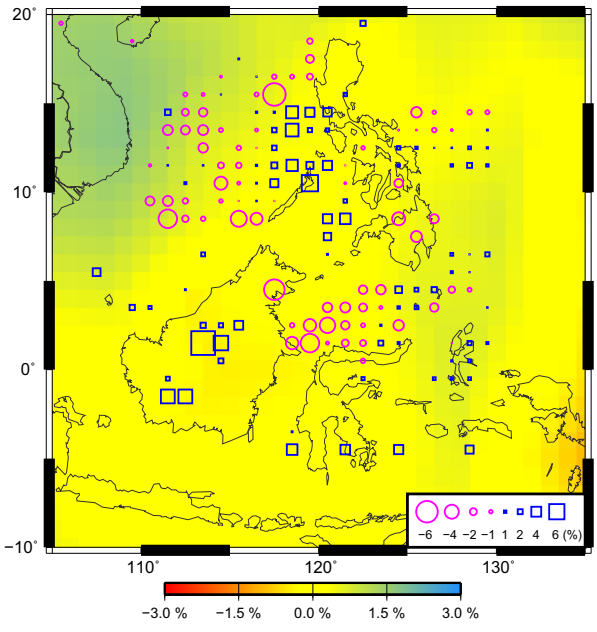

Fig. 4. Shear-velocity perturbations (symbols) inferred from the travel-time residuals in Fig. 3b and averaged over 1°× 1°grids. Positive perturbations are plotted as blue squares and negatives as red circles. Sizes of the symbols are proportional to magnitudes of shear-velocity perturbations. Background is shear-velocity perturbations at the CMB from GyPSuM model. (For interpretation of the references to color in this figure legend, the reader is referred to the web version of this article.)

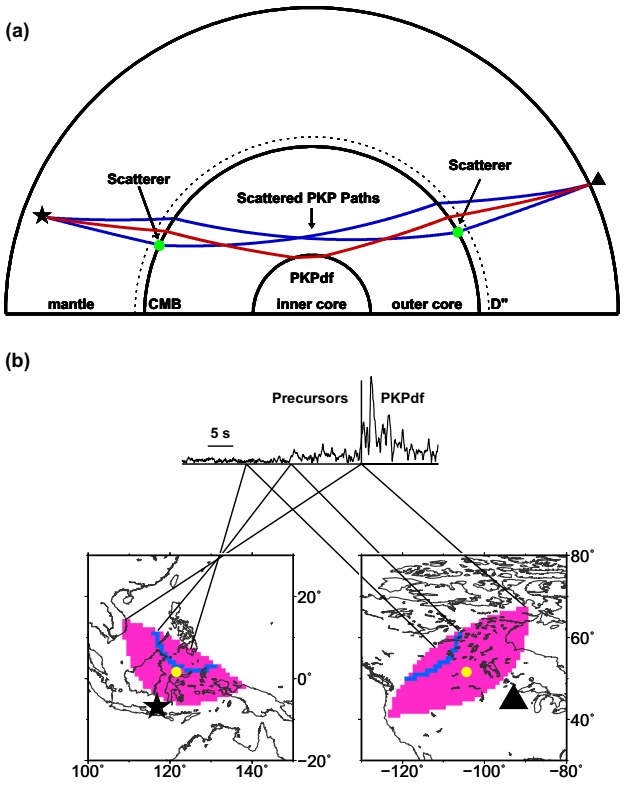

Fig. 5. (a) Ray paths of PKP precursors (blue lines) and PKPdf phase (red line) at a distance of 135° (triangle). PKPdf is the P wave propagating through the inner core. PKP precursors are the P waves deflected by seismic scatterers in the lower mantle beneath the source or/and the receiver (green circles) and becoming preceding PKPdf. Ray paths are calculated based on the reference model PREM (Dziewonski and Anderson, 1981) and a source (star) depth of 500 km. (b) Migration technique using PKP precursors to locate seismic scatterers in the lower mantle. The energy envelope of an observed vertical seismogram is shown in the middle of the figure. For an assumed depth of seismic scattering (the CMB in this example), the perspective scatterers producing the precursor onset energy are located in two "isotime scatterer arcs" (blue arcs) in the mantle beneath the source and the receiver. The precursor energy and the geographic locations of its associated perspective scatterers are connected by lines. Star and triangle represent event and station, respectively. Yellow circles indicate entry and exit points of the PKPdf ray at the CMB. (For interpretation of the references to color in this figure legend, the reader is referred to the web version of this article.)

3.1. PKP precursor data

We choose PKP precursor data recorded at the Transportable Array of the USArray. Only the PKP seismograms recorded at the distance range of 134–141° are used. PKP precursors at closer distances are insensitive to seismic scattering in the deep mantle and those recorded at larger distances would be affected by the energy from the PKP caustics (Wen, 2000). We search events occurring in the Sunda subduction zone from 2005 to 2012 with event depths larger than 100 km, and choose 20 high-quality events (events with superscript a Table 1). All selected PKP precursors exhibit large amplitudes and clear onsets (see an example in Fig. 6). All seismograms are filtered with the WWSSN short-period instrument response, which has a dominant frequency of about 1 Hz. The length scale of the seismic scatterers associated with this frequency range of PKP precursory energy is a few to 10′s km based on synthetic waveform modeling (Wen and Helmberger, 1998b).

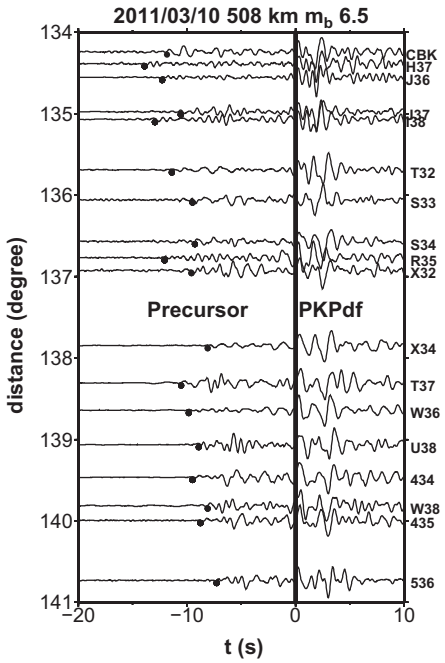

Fig. 6. An example of vertical displacements of PKP precursors and PKPdf phases observed at the USArray for event 2011/03/10, aligned along with the hand-picked PKPdf phase ($t = 0$). The hand-picked precursor onsets are indicated by circles. All traces are filtered with the WWSSN short-period instrument response.

3.2. Location of scattering energy near the CMB

We adopt a migration method developed by Wen (2000) to map the seismic scattering in the lowermost mantle based on the observed PKP precursory energy. We briefly review the method here. Readers are referred to Wen (2000) for details. For an assumed depth of scattering, PKP precursor energy arriving at a certain time can be caused by scatterers located along two "isotime scatterer arcs" (blue arcs, Fig. 5b) beneath both the source and the receiver in the lowermost mantle. The energy closer to the PKIKP arrival in time corresponds with the "isotime scatterer arcs" closer to the source and the receiver in geographic location. For a single PKP seismogram, it is impossible to distinguish between the source-side and receiver-side scatterers. Same is also true for scattering from the great-circle path and off-great circle path. However, with a dense seismic array such as USArray, one can accurately locate seismic scatterers. The migration method projects precursory energy observed at every seismic station back to possible scattering regions in the lower mantle. The scattering strengths at different depths and lateral locations are obtained by averaging the projected energy over an array of seismic observations.

The PKP precursors sample the lowermost mantle regions beneath Southeast Asia in the source side, and beneath Canada and western United States in the receiver side (Fig. 7). We discretize the regions into grids and test different depths of seismic scattering. For one assumed depth of scattering, we calculate "scatterer energy" and "hit counts" for each grid. The "scatterer energy" is defined as the ratio between the amplitudes of PKP precursors and the PKP phase, and is calculated following these procedures: (1) the precursor energy is assigned to a grid if the grid is situated in the "isotime scatterer arc" of the energy. Zero value is given otherwise; (2) while all seismic observations are considered together and their sampling patches overlay, grid values are averaged. As precursor amplitudes increase with increasing distance range, we correct all the precursor amplitudes to an epicentral distance of 138° (Hedlin et al., 1997). The "hit counts" at one particular grid is simply the total number of PKP precursor data sampling the grid. Grid scheme is chosen according to the uncertainties in hand-picking the PKIKP phases. The uncertainty of geographic location associated with this travel-time uncertainty depends on the epicentral distance of the receiver and the depth of seismic scattering. A 0.5 s error of time pick would result in uncertainties in geographic location at the CMB of about 18 km for a receiver at 131° and about 100 km for a receiver at 141°. We choose a grid scheme of $2 \times 2°$ after taking into account of the uncertainties due to a possible time pick error.

We test many depths of scatterering and present results of "scatterer energy" and "hit counts" for two assumed depths of seismic scattering: the CMB (Fig. 7b, c, f, g) and 200 km above the CMB (Fig. 7d, e, h, i). Both the source- and receiver-side mantle are well sampled by the PKP precursor data (Fig. 7f–i). Note that while there is also some scatterer energy in the receiver-side in the region with high hit-counts (Fig. 7c, e), it is much smaller than the scatterer energy in the source-side mantle (Fig. 7b, d). We thus infer that the seismic scattering lies in the source-side mantle. The scattering energy in the source-side mantle exhibits a crescent shape distributed from the South China Sea to the Maluku Islands (Fig. 7b). The inferred scatterer energy for the two assumed depths shows similar features with some differences in magnitude and distribution (Fig. 7b, d). The regions with strong seismic scatterer energy also have a large number of hit counts of PKP precursor sampling (Fig. 7f, h), indicating that the mapped energy pattern is a well-resolved feature, not an artifact of the migration process. We conclude that, based on the contrast of relative seismic energy between the source- and receive-side mantle and the large number of hit counts of the precursor sampling in the region, the mapped feature of seismic scatterer energy in the source-side mantle is well-resolved. However, there is little statistical difference between the scattering at the CMB and that 200 km above the CMB in the source-side mantle (Fig. 7b, d).

3.3. Velocity perturbation of seismic scatterers

While the observed PKP precursors can be accurately tracked back to the CMB region from the South China Sea to the Maluku Islands (Fig. 7b), it is difficult to use the precursor amplitudes to constrain the magnitude of seismic heterogeneities. The amplitude of PKP precursors is affected by many characteristics of seismic scatterers: magnitude, wavelength and geometry. Seismic scatterers with a large velocity perturbation may still produce weak precursors, if seismic precursors sample the seismic structures in a less optimal geometry (Wen, 2000).

Nevertheless, the observed strong PKP precursory energy is comparable with that observed in the NORSAR array (Vidale and Hedlin, 1998), at stations TAB and UME of the Global Seismic Network (Wen and Helmberger, 1998b) and in a Tanzania regional seismic network (Wen, 2000). All these previous studies have indicated that the anomalously strong PKP precursory energy would require significant velocity perturbations in the lowermost mantle. For example, Vidale and Hedlin (1998) showed that anomalous large PKP precursors from earthquakes in northern Tonga required strong 10–15% r.m.s. P velocity variations near the CMB below Tonga; Wen and Helmberger (1998b) indicated that their observed long-period PKP precursors required P velocity drops of at least 7% at the bottom of the mantle; and Wen (2000) suggested that a P velocity variation of at least 8% was required to produce scattering energy observed at station KIBE from a Fiji event. We conclude that the anomalously strong PKP precursory energy in this study would require similar magnitude of velocity perturbation in the lowermost mantle.

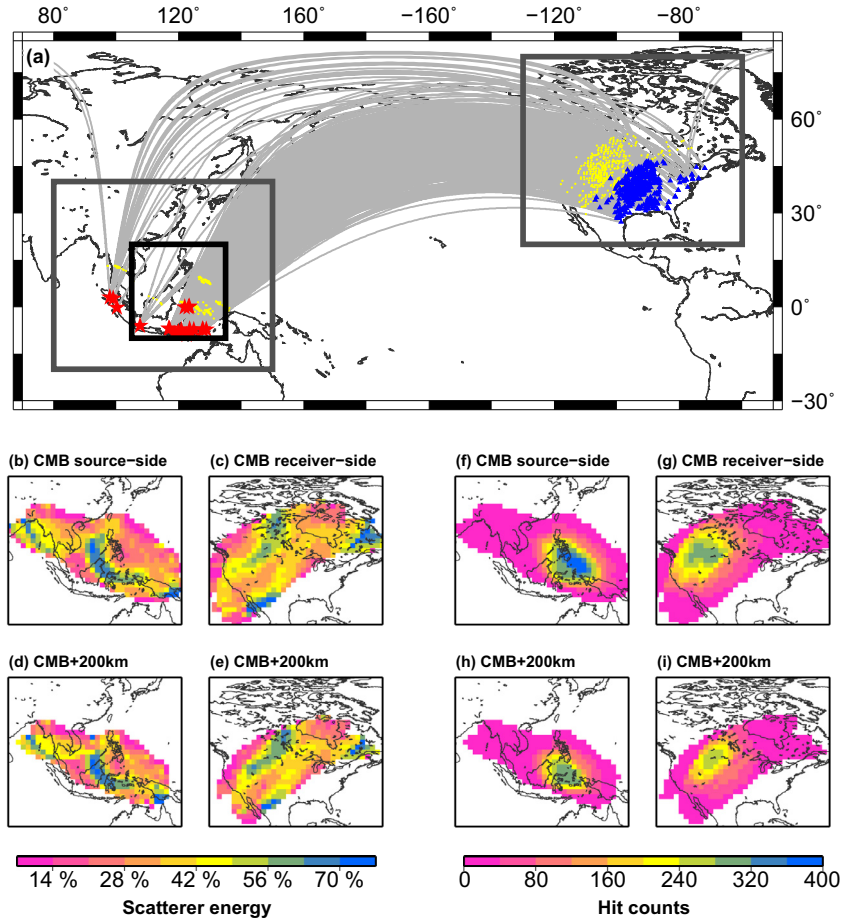

Fig. 7. (a) Great-circle paths (gray lines), PKPdf entry and exit points on the CMB (yellow dots), earthquake (red stars) and seismic stations at the USArray (blue triangles) for the PKP precursor study. Two large dark gray boxes indicate the regions where the PKP scattering mapping results are presented in the bottom panels (b–i). Small black box indicates the study region where the inferred shear-velocity structure and seismic scattering are present in Fig. 8. (b–e) Maps of "scatterer energy" and (f–i) "hit counts" (see text for explanation). Two depths of seismic scattering are assumed: the CMB (top row) and 200 km above the CMB (bottom row). (For interpretation of the references to color in this figure legend, the reader is referred to the web version of this article.)

4. Origin of seismic structure at the base of the mantle beneath Southeast Asia

The region of strong scattering (with scattering energy greater than 50%) is distributed from the South China Sea to the Maluku Islands and coincides with the western edge of the low shear-velocity region (Figs. 7b, d and 8a). The correspondence of strong scattering with a low-velocity region suggests that the seismic scattering is caused by ULVZs in the region. The inferred western-most low-velocity region could be consistent with either just a ridge of ULVZs with extremely large velocity reductions or a scenario that a low-velocity region with ULVZs situating at its base.

Idehara et al. (2007) and Idehara (2011) reported existence of ULVZ in some region of the study area and lack of evidence for ULVZ in some other region, based on stacked ScP waveforms. Some of their reported regions with ULVZ exhibit strong scattering from the PKP data in this study (e.g., north of the Kalimantan Island), but some regions do not (e.g., east of Philippine). Similarly, some of their reported regions of no ULVZ evidence exhibit little scattering from our PKP data (e.g., middle of the Sulawesi Sea), but some regions do (e.g., the South China Sea). The difference probably lies on the sampling abilities of the two different datasets and assumptions made in the studies. The technique of ScP studies is more sensitive to flat ULVZ which emphasizes the coherent energy from the stacked ScP seismograms, while the PKP precursor is related to the seismic structures with geometry as PKP precursory energy comes from the seismic wave deflected from the PKP ray paths. Moreover, the ScP mapping of ULVZ was performed assuming one-dimensional wave propagation and ULVZ was assumed located at the ScP bouncing point at the CMB, while the ScP precursory and post-cursory energy may actually come from far away from the ScP bouncing point or off great circle paths. On the other hand, a strong ULVZ may also produce weak PKP precursory energy if PKP waves sample the ULVZ in a less optimal geometry, rendering it undetectable from PKP precursor data (Wen, 2000).

Our selection of ScP data is primarily for the purpose of complementing the travel-time sampling of ScS phases in the region, not for studying ULVZ. Some selected events are shallow focus, exhibiting complex waveforms from shallow crustal reverberations, not useful for studying ULVZ. The only five deep events in our selection show a simple source time function and two of them exhibit evidence of ULVZ. The observed absence and presence of ULVZ evidence in our data are consistent with Idehara et al. (2007) and do not add more additional sampling to their studies.

It is interesting to note that the velocity structure in the northeast of the region exhibits a complex geographic pattern with several alternate low- and high-velocity patches adjacent to each other. One possible explanation of the seismic structure in this region is that the region represents a complex interaction between a downwelling and a low-velocity region near the CMB (Fig. 8b). The downwelling (the high-velocity patches) displaces the low-velocity region into many low-velocity patches and pushes the

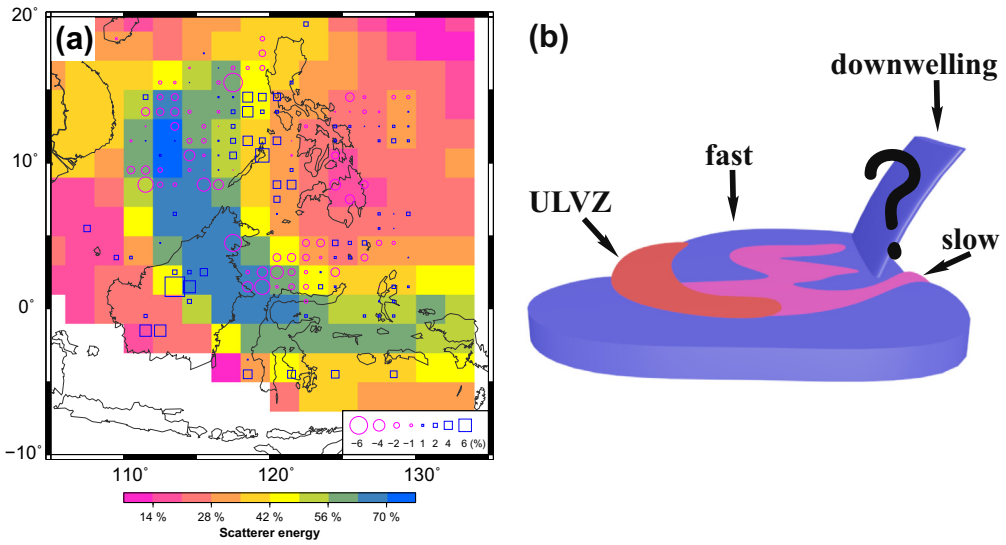

Fig. 8. (a) Scatterer energy at the CMB (color background) along with shear-velocity perturbations in the lowermost 200 km of the mantle (symbols) from Fig. 4. (b) Cartoon illustrating a possible complex interaction between a downwelling (blue areas) and a low-velocity region (red and pink areas) in the lowermost 200 km of the mantle. The downwelling displaces the low-velocity region into many low-velocity patches (pink areas) and pushes the ULVZs (red ridge) to the edge of the low-velocity region. The low-velocity region is also surrounded by high-velocity regions, also possibly related to downwellings. (For interpretation of the references to color in this figure legend, the reader is referred to the web version of this article.)

ULVZs to the edge of the low-velocity region surrounded by high-velocity regions. In this scenario, the ULVZs near the edge exhibit strong seismic scattering, while the velocity structure in the northeast exhibits a complex distribution of low- and high-velocity patches, but with little seismic scattering.

5. Conclusions

Using ScS travel-time residuals and ScS-S and ScP-P differential travel-time residuals, we constrain the average shear-velocity structure near the CMB beneath Southeast Asia. The inferred average velocity perturbations in the lowermost 200 km of the mantle range from about −6% to 6% and exhibit a complex geographic distribution of alternate low- and high-velocity patches adjacent to each other, surrounded by a high-velocity anomaly in the south. Using the observed PKP precursory energy, we map seismic scatterering in the region. The seismic scatterers exhibit a crescent shape distributed from the South China Sea to the Maluku Islands with large velocity perturbations. The geographic distribution of seismic scatterers coincides with the westernmost low-velocity patches, suggesting that the seismic scattering is caused by ULVZs in the region. We suggest that the seismic structure in the region likely results from a complex interaction between a downwelling and a low-velocity region near the CMB. The downwelling (the high-velocity patches) displaces the low-velocity region into many low-velocity patches and pushes the ULVZs to the edge of the low-velocity region. The ULVZs at the edge exhibit as a low-velocity ridge and strong seismic scattering, while the velocity structure in the northeast region exhibits a complex distribution of low- and high-velocity patches, but with little seismic scattering.

Acknowledgments

We gratefully acknowledge the participants of the CENC, the F-net, the IRIS and the USArray for their efforts in collecting the high-quality data. We thank Satoru Tanaka and one anonymous reviewer for comments and suggestions that improved the paper significantly. This work is supported by the National Natural Science Foundation of China under grant NSFC41130311 and the Chinese Academy of Sciences and State Administration of Foreign Experts Affairs International Partnership Program for Creative Research Teams.

References

Avants, M., Lay, T., Garnero, E.J., 2006. A new probe of ULVZ S-wave velocity structure: array stacking of ScS waveforms. Geophys. Res. Lett. 33, L07314.
Cleary, J., Haddon, R., 1972. Seismic wave scattering near the core-mantle boundary: a new interpretation of precursors to PKP. Nature 240, 549–551.
Cormier, V.F., 1999. Anisotropy of heterogeneity scale lengths in the lower mantle from PKIKP precursors. Geophys. J. Int. 136, 373–384.
Cottaar, S., Romanowicz, B., 2012. An unsually large ULVZ at the base of the mantle near Hawaii. Earth Planet. Sci. Lett. 355, 213–222.
Doornbos, D., Husebye, E., 1972. Array analysis of PKP phases and their precursors. Phys. Earth Planet. In. 5, 387–399.
Dziewonski, A.M., Anderson, D.L., 1981. Preliminary reference Earth model. Phys. Earth Planet. In. 25, 297–356.
Frost, D.A., Rost, S., Selby, N.D., Stuart, G.W., 2013. Detection of a tall ridge at the core-mantle boundary from scattered PKP energy. Geophys. J. Int. 195, 558–574.
Garnero, E.J., 2000. Heterogeneity of the lowermost mantle. Annu. Rev. Earth Planet. Sci. 28, 509–537.
Garnero, E.J., Helmberger, D.V., 1995. A very slow basal layer underlying large-scale low-velocity anomalies in the lower mantle beneath the Pacific: evidence from core phases. Phys. Earth Planet. In. 91, 161–176.
Garnero, E.J., Vidale, J.E., 1999. ScP: a probe of ultralow velocity zones at the base of the mantle. Geophys. Res. Lett. 26, 377–380.
Haddon, R., Cleary, J., 1974. Evidence for scattering of seismic PKP waves near the mantle-core boundary. Phys. Earth Planet. In. 8, 211–234.
He, Y., Wen, L., 2009. Structural features and shear-velocity structure of the "Pacific Anomaly". J. Geophys. Res. 114, B02309.
He, Y., Wen, L., 2012. Geographic boundary of the "Pacific Anomaly" and its geometry and transitional structure in the north. J. Geophys. Res.: Solid Earth 117, B09308.
He, Y., Wen, L., Zheng, T., 2006. Geographic boundary and shear wave velocity structure of the "Pacific anomaly" near the core-mantle boundary beneath western Pacific. Earth Planet. Sci. Lett. 244, 302–314.
Hedlin, M.A., Shearer, P.M., Earle, P.S., 1997. Seismic evidence for small-scale heterogeneity throughout the Earth's mantle. Nature 387, 145–150.
Helmberger, D., Ni, S., Wen, L., Ritsema, J., 2000. Seismic evidence for ultralow-velocity zones beneath Africa and eastern Atlantic. J. Geophys. Res.: Solid Earth 105, 23865–23878 (1978–2012).
Helmberger, D., Wen, L., Ding, X., 1998. Seismic evidence that the source of the Iceland hotspot lies at the core-mantle boundary. Nature 396, 251–255.
Husebye, E., King, D., Haddon, R., 1976. Precursors to PKIKP and seismic wave scattering near the mantle-core boundary. J. Geophys. Res. 81, 1870–1882.
Hutko, A.R., Lay, T., Revenaugh, J., 2009. Localized double-array stacking analysis of PcP: D″ and ULVZ structure beneath the Cocos plate, Mexico, central Pacific, and north Pacific. Phys. Earth Planet. In. 173, 60–74.

Idehara, K., 2011. Structural heterogeneity of an ultra-low-velocity zone beneath the Philippine Islands: implications for core-mantle chemical interactions induced by massive partial melting at the bottom of the mantle. Phys. Earth Planet. In. 184, 80–90.
Idehara, K., Yamada, A., Zhao, D., 2007. Seismological constraints on the ultralow velocity zones in the lowermost mantle from core-reflected waves. Phys. Earth Planet. In. 165, 25–46.
Jensen, K.J., Thorne, M.S., Rost, S., 2013. SPdKS analysis of ultralow-velocity zones beneath the western Pacific. Geophys. Res. Lett. 40, 4574–4578.
Mao, W.L., Mao, H., Sturhahn, W., Zhao, J., Prakapenka, V.B., Meng, Y., Shu, J., Fei, Y., Hemley, R.J., 2006. Iron-rich post-perovskite and the origin of ultralow-velocity zones. Science 312, 564–565.
McNamara, A.K., Garnero, E.J., Rost, S., 2010. Tracking deep mantle reservoirs with ultra-low velocity zones. Earth Planet. Sci. Lett. 299, 1–9.
Mori, J., Helmberger, D.V., 1995. Localized boundary layer below the mid-Pacific velocity anomaly identified from a PcP precursor. J. Geophys. Res.: Solid Earth 100, 20359–20365.
Niu, F., Wen, L., 2001. Strong seismic scatterers near the core-mantle boundary west of Mexico. Geophys. Res. Lett. 28, 3557–3560.
Rondenay, S., Cormier, V.F., Van Ark, E.M., 2010. SKS and SPdKS sensitivity to two-dimensional ultralow-velocity zones. J. Geophys. Res.: Solid Earth 115, B04311.
Rost, S., Garnero, E.J., Williams, Q., Manga, M., 2005. Seismological constraints on a possible plume root at the core-mantle boundary. Nature 435, 666–669.
Rost, S., Revenaugh, J., 2003. Small-scale ultralow-velocity zone structure imaged by ScP. J. Geophys. Res.: Solid Earth 108 (B1), 2056.
Simmons, N.A., Forte, A.M., Boschi, L., Grand, S.P., 2010. GyPSuM: a joint tomographic model of mantle density and seismic wave speeds. J. Geophys. Res.: Solid Earth 115, B12310.
Thomas, C., Weber, M., Wicks, C.W., Scherbaum, F., 1999. Small scatterers in the lower mantle observed at German broadband arrays. J. Geophys. Res.: Solid Earth 104, 15073–15088.
Thorne, M.S., Garnero, E.J., 2004. Inferences on ultralow-velocity zone structure from a global analysis of SPdKS waves. J. Geophys. Res.: Solid Earth 109, B08301.
Thorne, M.S., Garnero, E.J., Jahnke, G., Igel, H., McNamara, A.K., 2013. Mega ultra low velocity zone and mantle flow. Earth Planet Sci. Lett. 364, 59–67.
Vidale, J.E., Hedlin, M.A., 1998. Evidence for partial melt at the core-mantle boundary north of Tonga from the strong scattering of seismic waves. Nature 391, 682–685.
Wang, Y., Wen, L., 2007. Geometry and P and S velocity structure of the "African Anomaly". J. Geophys. Res.: Solid Earth 1978–2012, 112.
Wen, L., 2000. Intense seismic scattering near the Earth's core-mantle boundary beneath the Comoros hotspot. Geophys. Res. Lett. 27, 3627–3630.
Wen, L., 2001. Seismic evidence for a rapidly varying compositional anomaly at the base of the Earth's mantle beneath the Indian Ocean. Earth Planet. Sci. Lett. 194, 83–95.
Wen, L., 2002. An SH hybrid method and shear velocity structures in the lowermost mantle beneath the central Pacific and South Atlantic Oceans. J. Geophys. Res.: Solid Earth 107 (B3), 2055.
Wen, L., Helmberger, D.V., 1998a. A two-dimensional P-SV hybrid method and its application to modeling localized structures near the core-mantle boundary. J. Geophys. Res.: Solid Earth 103, 17901–17918.
Wen, L., Helmberger, D.V., 1998b. Ultra-low velocity zones near the core-mantle boundary from broadband PKP precursors. Science 279, 1701–1703.
Wicks, J.K., Jackson, J.M., Sturhahn, W., 2010. Very low sound velocities in iron-rich (Mg, Fe)O: Implications for the core-mantle boundary region. Geophys. Res. Lett. 37, L15304.
Williams, Q., Garnero, E.J., 1996. Seismic evidence for partial melt at the base of Earth's mantle. Science 273, 1528–1530.
Williams, Q., Revenaugh, J., Garnero, E., 1998. A correlation between ultra-low basal velocities in the mantle and hot spots. Science 281, 546–549.
Xu, Y., Koper, K.D., 2009. Detection of a ULVZ at the base of the mantle beneath the northwest Pacific. Geophys. Res. Lett. 36, L17301.
Zhang, Y., Ritsema, J., Thorne, M.S., 2009. Modeling the ratios of SKKS and SKS amplitudes with ultra-low velocity zones at the core-mantle boundary. Geophys. Res. Lett. 36, L19303.